

# Langmuir–Blodgett Nanowire Devices for In Situ Probing of Zinc-Ion Batteries

Qin Liu, Zhimeng Hao, Xiaobin Liao, Xuelei Pan, Shuxuan Li, Lin Xu,\* and Liqiang Mai

In situ monitoring the evolution of electrode materials in micro/nano scale is crucial to understand the intrinsic mechanism of rechargeable batteries. Here a novel on-chip Langmuir–Blodgett nanowire (LBNW) microdevice is designed based on aligned and assembled MnO<sub>2</sub> nanowire quasimonolayer films for directly probing Zn-ion batteries (ZIBs) in real-time. With an interdigital device configuration, a splendid Ohmic contact between MnO<sub>2</sub> LBNWs and pyrolytic carbon current collector is demonstrated here, enabling a small polarization voltage. In addition, this work reveals, for the first time, that the conductance of MnO<sub>2</sub> LBNWs monotonically increases/decreases when the ZIBs are charged/discharged. Multistep phase transition is mainly responsible for the mechanism of the ZIBs, as evidenced by combined high-resolution transmission electron microscopy and in situ Raman spectroscopy. This work provides a new and adaptable platform for microchip-based in situ simultaneous electrochemical and physical detection of batteries, which would promote the fundamental and practical research of nanowire electrode materials in energy storage applications.

system containing several scientific issues that are still ambiguous, for instance, real-time structural evolution, changing electrical conductance, solid-solid interface between electrode materials and current collectors, etc. Hence, real-time monitoring of the electrochemical processes in micro/nano scale would lead to further development of high-performance electrode materials.

In previous researches, the single-nanowire electrochemical device has been conducted for in situ probing of the electrochemical processes and battery behaviors to investigate the intrinsic mechanism.<sup>[20]</sup> Compared with traditional in situ detecting systems, the single-nanowire electrochemical device can effectively avoid introducing binders and conductive carbon additives. However, such powerful detecting tools still have several limitations. First, the single nano-


wire devices are extremely demanding in terms of accuracy for the instrument owing to the large interface impedance (estimated at ~tens of gigaohms).<sup>[20]</sup> Second, the detected signals of the single nanowire are weak due to their dinky size.

In order to overcome the aforementioned limitations and make further extension, a novel on-chip in situ characterization device is designed (schematically illustrated in **Figure 1a**). This device is consisted of aligned nanowire monolayer film as working electrode (WE) and ultrafine zinc rod as counter/reference electrodes (CE/RE). The schematic circuit diagram of the device allowing in situ monitoring of electrochemical and electrical transport measurements is illustrated in **Figure 1b**. Interdigital microelectrodes are adopted and a bias voltage ( $V_{SD}$ ) is applied to measure the electrical transport property during charging/discharging processes. In detail, Langmuir–Blodgett nanowires (LBNWs) are linked with interdigital microelectrodes (source and drain), and a constant bias voltage ( $V_C$ ) is applied during the cyclic voltammetry (CV) measurements. The source–drain current and the Faradic current through zinc rod for in-device CV is recorded during the measurement. Meanwhile, Raman spectra is applied to measure the structural evolution during charge/discharge processes. In particular, the aligned LBNW film electrode has several unique advantages. First, it avoids the interference from binder and conductive additive to uncover the intrinsic evolution mechanism of electrode materials. Second, it enhances the detecting electrical and electrochemical signals compared to the single nanowire electrochemical devices. Third, single-crystalline nanowires are

## 1. Introduction

The increasingly worsening environmental pollution and the ever-growing energy consumption have incited strong interests on the high-performance energy storage system with good safety and high environmental friendliness.<sup>[1–5]</sup> Various types of rechargeable battery technologies have been developed to meet the critical demands of energy consumption.<sup>[6–8]</sup> Compared with lithium-ion batteries, rechargeable aqueous Zn-ion batteries (ZIBs), especially Zn-MnO<sub>2</sub> batteries,<sup>[4,9–11]</sup> become a hotspot due to their distinctive advantages of cost effectiveness, environmental friendly nature, and materials abundance. To date, intensive efforts have been devoted into exploring high-performance aqueous ZIBs.<sup>[12–18]</sup> Physical and chemical changes of electrode materials in Zn-MnO<sub>2</sub> batteries after cycling have been revealed through ex situ characterization techniques.<sup>[4,10,19]</sup> However, aqueous ZIB is a complicated

Q. Liu, Z. M. Hao, X. B. Liao, X. L. Pan, S. X. Li, Prof. L. Xu, Prof. L. Q. Mai  
State Key Laboratory of Advanced Technology for Materials Synthesis and Processing  
International School of Materials Science and Engineering  
Wuhan University of Technology  
Wuhan 430070, P. R. China  
E-mail: linxu@whut.edu.cn

 The ORCID identification number(s) for the author(s) of this article can be found under <https://doi.org/10.1002/sml.201902141>.

DOI: 10.1002/sml.201902141

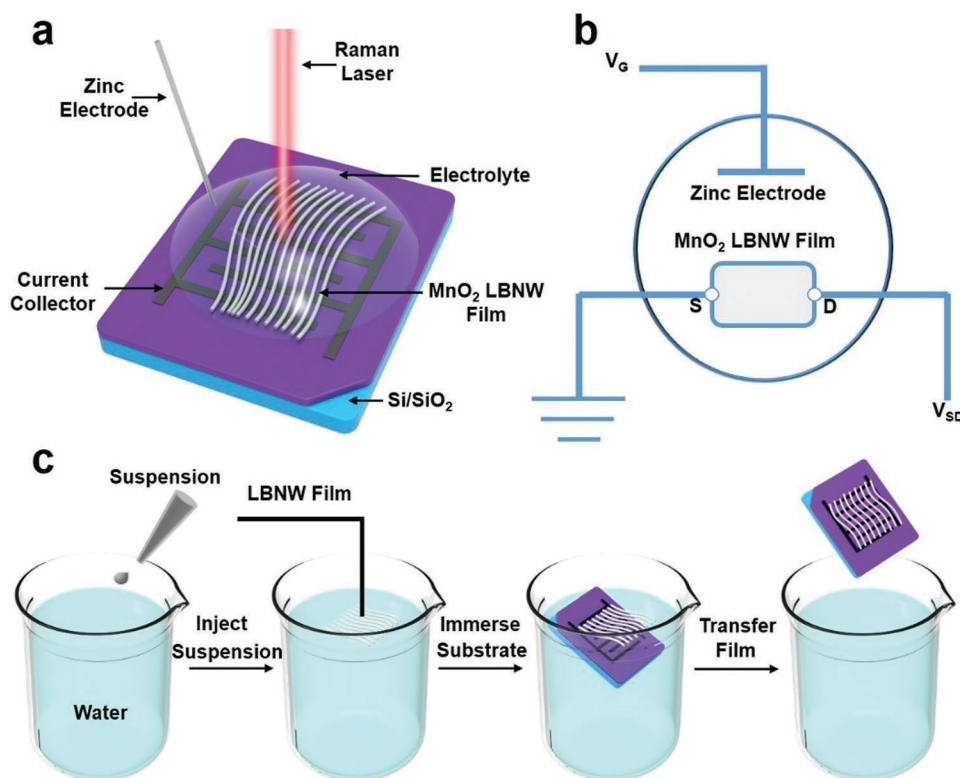


**Figure 1.** Schematic diagram of the LBNW device layout. a) The overview of the device. The  $\text{MnO}_2$  LBNW film and ultrafine zinc rod work as the working electrode and counter/reference electrode, respectively.  $\text{ZnSO}_4$  solution with and without  $\text{MnSO}_4$  additive are applied as the electrolyte. b) Schematic diagram of in-device CV and Raman for in situ probing the electrochemical processes. S, source; D, drain. c) Schematic illustration of the LBS assembling processes.

aligned across the interdigital electrodes which can represent the intrinsic property of single nanowire. Last, the monolayer characteristics can facilitate sufficient electrochemical reaction and accurate signal detecting.

To realize this device fabrication, two key issues should be addressed in advance, including: 1) can the  $\text{MnO}_2$  nanowires be assembled into ordered monolayer film for enhancing the in situ monitoring of signals; and 2) can a low interface impedance be formed between the nanowires and the current collectors to avoid the influence on electrochemical property? Herein, we address those above two major problems by the following strategies before assembling the devices. First, we propose a simple Langmuir–Blodgett process referred to as Langmuir–Blodgett scooping (LBS) which can realize self-assembly of  $\text{MnO}_2$  nanowires instead of applying mechanical forces to chaotic materials at the air/water interface. Notably, it is revealed that homogeneous LBNWs floated on a nonreactive substrate in aqueous media can be easily transferred to silicon wafer. Second, electrical contact characteristics are explored between  $\text{MnO}_2$  LBNWs and various patternable current collectors by measuring the  $I$ – $V$  curves.

## 2. Results and Discussion

$\text{MnO}_2$  nanowires were synthesized via a hydrothermal method referred to the previous work.<sup>[9]</sup> Figure S2 (Supporting

Information) shows the structure and morphology of the uniform  $\text{MnO}_2$  nanowires ( $\approx 40$  nm in diameter and  $\approx 10$   $\mu\text{m}$  in length). The as-prepared  $\text{MnO}_2$  nanowires were assembled into a well-packed film by LBS method (Figure 1c), which is more convenient and faster than the conventional Langmuir–Blodgett method.<sup>[21–24]</sup> Water presents a larger surface tension ( $7.19 \times 10^{-2}$   $\text{N m}^{-1}$ ) than *n*-butanol ( $4.45 \times 10^{-2}$   $\text{N m}^{-1}$  at 0.2 M) at 25 °C, resulting in a surface tension gradient.<sup>[25]</sup> This allows *n*-butanol to spread evenly on the water surface,<sup>[25,26]</sup> driving the  $\text{MnO}_2$  nanowires to expand around and neatly arranged. In short, a turbulent injection of a water-miscible solvent at the water–air interface induces a strong surface flow which drives the solvent diffusion, namely Marangoni effect.<sup>[27]</sup> Briefly, interdigital electrodes on silicon wafer were fabricated via a typical photolithography process (Figure S1, Supporting Information). Then a mixed suspension was obtained by dispersing  $\text{MnO}_2$  nanowires (0.2 mg) in ethanol (500  $\mu\text{L}$ ), *n*-butanol (300  $\mu\text{L}$ ), and pure deionized water (600  $\mu\text{L}$ ). After sonication treatment for 30 min, the as-prepared suspension was added dropwise into a beaker (50 mL) full of deionized water. After that, an aligned  $\text{MnO}_2$  quasimonolayer film is formed on the surface of the solution and then transferred to the silicon wafer (Figure 2a).

Electron transport and ultraviolet photoelectron spectroscopy (UPS) at the interface of current collector/ $\text{MnO}_2$  heterostructures were investigated in an effort to seek for an appropriate current collector to guarantee Ohmic contact and minimum

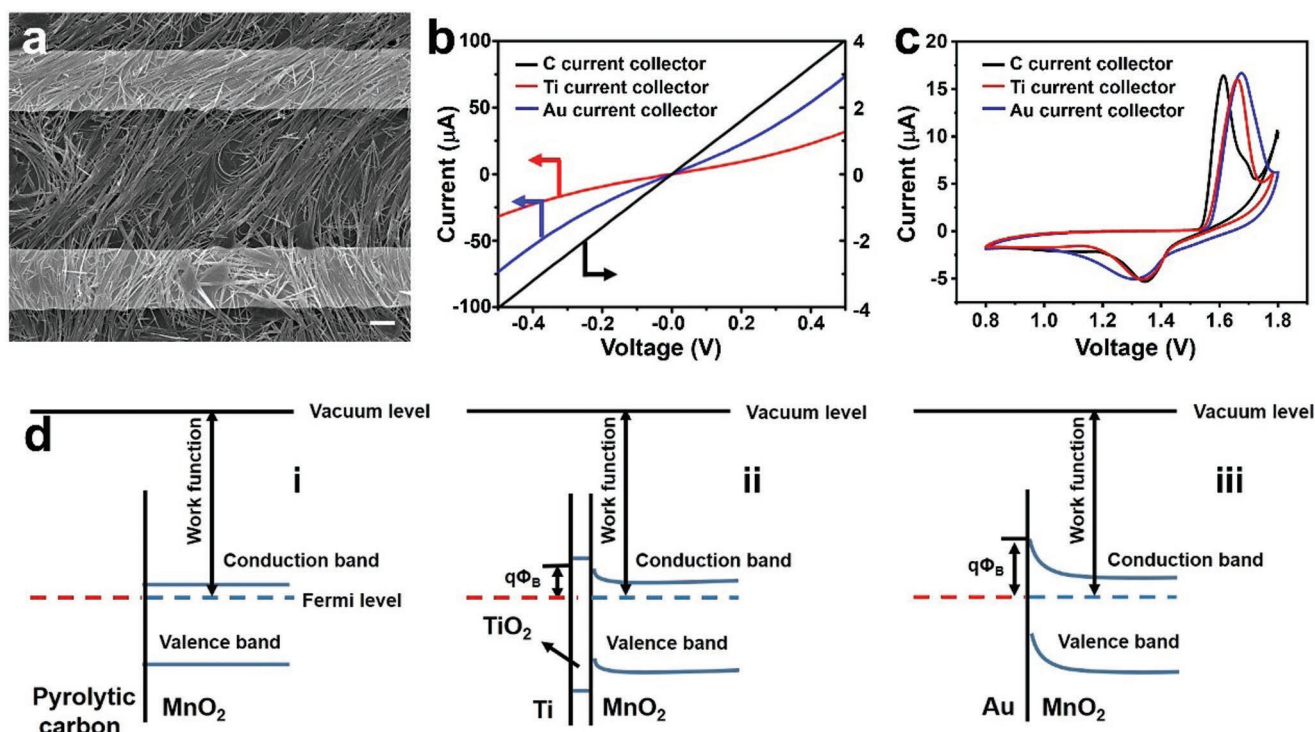


**Figure 2.** Characterization of LBNW film. a) SEM image of original LBNW film deposit on pyrolytic carbon interdigital electrode. Scale bar, 2  $\mu\text{m}$ . b)  $I$ - $V$  curves of LBNW film with three representative current collector materials including Ti, Au, and pyrolytic carbon. c) CV curves ( $2 \text{ mV s}^{-1}$ , second cycle) of LBNW film with Ti, Au, and pyrolytic carbon current collectors in  $\text{ZnSO}_4$  electrolyte with preadded  $\text{Mn}^{2+}$ . d) The schematic diagram of the band alignment at the interface of i) pyrolytic carbon/ $\text{MnO}_2$ , ii) Ti/ $\text{MnO}_2$ , and iii) Au/ $\text{MnO}_2$ .

impedance. (Figure 2; Figure S3, Supporting Information). Three types of current collectors, Ti, Au, and pyrolytic carbon, were employed to investigate the interface characteristics between electrode materials and current collectors, as they are frequently used to manufacture energy storage microdevices. The reported  $\alpha\text{-MnO}_2$  is a typical n-type semiconductor with a work function of 4.40 eV,<sup>[28]</sup> much smaller than the work function of Au ( $\approx 5.1 \text{ eV}$ ) and Ti ( $\approx 4.8 \text{ eV}$ ), which predicts that the electrons should flow from  $\alpha\text{-MnO}_2$  side to metal side to realign the Fermi level once the metals and semiconductor contact. Therefore, i) the semiconductor  $\alpha\text{-MnO}_2$  is depleted near the interfaces and the Schottky barriers form at the interfaces. ii) the Schottky barrier height  $\Phi_{\text{B}} = \Phi_{\text{metal}} - \chi_{\text{semi}}$ , where  $\Phi_{\text{metal}}$  is work function of the metal, and  $\chi_{\text{semi}}$  is the vacuum electron affinity of  $\alpha\text{-MnO}_2$ . The barrier height at Au/ $\text{MnO}_2$  interface should be higher than that at Ti/ $\text{MnO}_2$  interface. The  $I$ - $V$  curves of  $\text{MnO}_2$  nanowires with Ti and Au as electrodes demonstrate the nonlinear behavior, proving the existence of the large Schottky barriers at interfaces (Figure 2b). In UPS measurement, the work function of measured material can be obtained via  $\Phi = E_{\text{hv}} - E_{\text{cutoff}}$ , where  $E_{\text{hv}}$  is photon energy of the He source ( $\approx 21.2 \text{ eV}$ ), and  $E_{\text{cutoff}}$  is the measured energy of the secondary electron cutoff. The measured  $E_{\text{cutoff}}$  in Au/ $\alpha\text{-MnO}_2$ , Ti/ $\alpha\text{-MnO}_2$ , and pyrolytic carbon/ $\alpha\text{-MnO}_2$  systems, are approaching to 16.4 eV and the calculated work function  $\Phi_{\alpha\text{-MnO}_2}$  is  $\approx 4.8 \text{ eV}$  (Figure 2d; Figure S3, Supporting Information). The work function of  $\alpha\text{-MnO}_2$  is close to that of Ti, which indicates that the  $\alpha\text{-MnO}_2$  and Ti can form Ohmic contact, inconsistent with  $I$ - $V$  measurement. The reason may

be that a dense  $\text{TiO}_x$  film commonly exists on Ti metal should introduce additional Schottky barrier. The work function of multiwalled carbon tubes were reported in the range from 4.1 to 4.7 eV.<sup>[29]</sup> Both the UPS measurement and  $I$ - $V$  measurement demonstrate that Ohmic contact has formed at pyrolytic carbon/ $\alpha\text{-MnO}_2$  interface, which indicates the work function of pyrolytic carbon is close or smaller than that of  $\alpha\text{-MnO}_2$ .

In order to further explore the effect of interface impedance and barrier on the electrochemical properties of the materials, CV measurements of the devices based on Ti, Au, and pyrolytic carbon current collectors were conducted (Figure 2c). There are two distinguishable peaks at around 1.3 and 1.7 V versus  $\text{Zn}^{2+}/\text{Zn}$  during cycling. Obviously, the ZIBs own the minimum polarization when pyrolytic carbon is used as a current collector, indicating that the formation of Ohmic contacts can effectively optimize the polarization of electrode materials. Overall, pyrolytic carbon is discovered to form good Ohmic contact with the  $\text{MnO}_2$  LBNWs and can effectively reduce the electrochemical polarization. In addition, the aligned LBNWs possess a higher conductance and similar polarization voltage compared to messy nanowires (Figure S4, Supporting Information).

After successfully addressing the above two key issues: 1) aligned LBNW quasimonolayer film assembly and 2) formation of Ohmic contact between LBNWs and current collector, we fabricated LBNW devices with pyrolytic carbon current collector for in situ probing of ZIBs. Most importantly, two types of electrolytes, pure  $\text{ZnSO}_4$  electrolyte and  $\text{ZnSO}_4$  electrolyte with  $\text{MnSO}_4$  additive are proposed to explore the influence of the preadded  $\text{Mn}^{2+}$ .  $I$ - $V$  curves were carried out to investigate

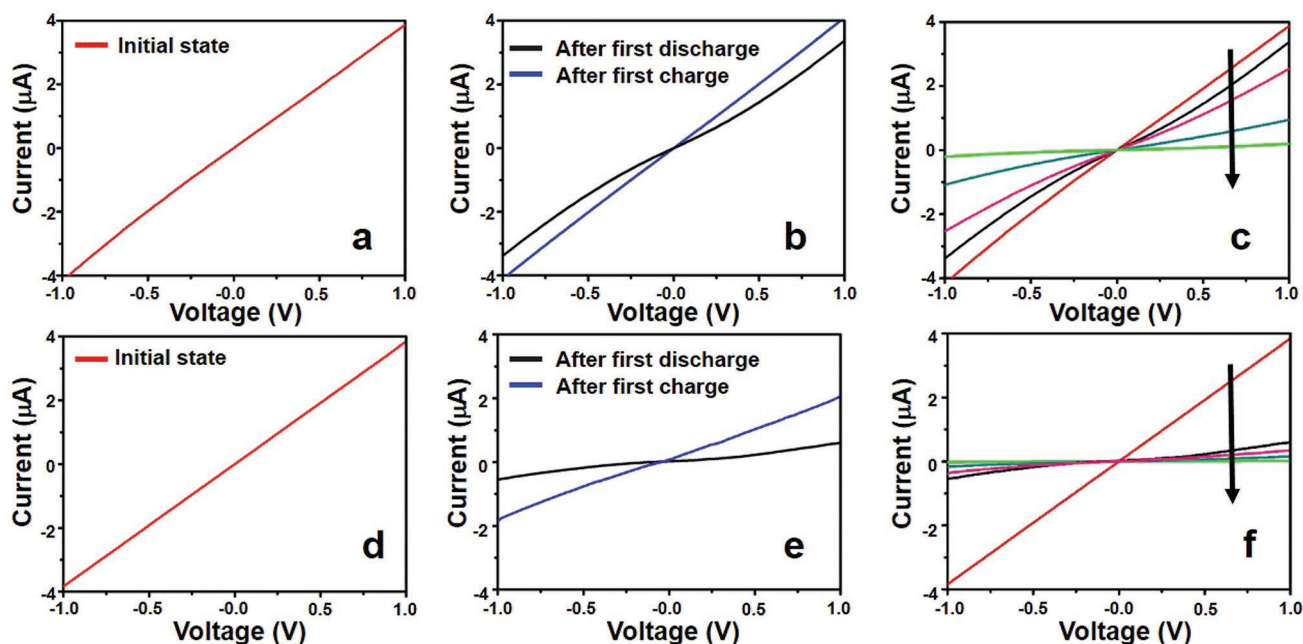


**Figure 3.** In situ transport characterization of LBNW devices. a)  $I$ - $V$  curve of  $\text{MnO}_2$  LBNWs at initial state. b)  $I$ - $V$  curves of  $\text{MnO}_2$  LBNWs after first galvanostatic charging/discharging process at  $1 \mu\text{A cm}^{-2}$ . c)  $I$ - $V$  curves of  $\text{MnO}_2$  LBNWs along with electrochemical cycling.  $I$ - $V$  curves in a-c) are tested in  $2 \text{ M ZnSO}_4$  electrolyte with  $0.1 \text{ M MnSO}_4$  additive. d)  $I$ - $V$  curve of  $\text{MnO}_2$  LBNWs at initial state. e)  $I$ - $V$  curves of  $\text{MnO}_2$  LBNWs after first galvanostatic charging/discharging process at  $1 \mu\text{A cm}^{-2}$ . f)  $I$ - $V$  curves of  $\text{MnO}_2$  LBNWs along with electrochemical test.  $I$ - $V$  curves in (d-f) are tested in  $2 \text{ M pure ZnSO}_4$  electrolyte. Colors in (c,f) mean as follows: red, initial state; black, after 10 galvanostatic charging; dark cyan, after 50 galvanostatic charging; green, after 375 galvanostatic charging.

the electrical transport of  $\text{MnO}_2$  LBNWs during the charging/discharging processes (Figure 3; Figure S5, Supporting Information). Initially,  $\text{MnO}_2$  LBNWs have a relatively high conductance (Figure 3a,d). After the first galvanostatic charging process at  $1 \mu\text{A cm}^{-2}$  in the voltage range of  $0.8$ – $1.8 \text{ V}$ , the conductance of  $\text{MnO}_2$  LBNWs was decreased in both electrolytes (Figure 3b,e). In detail, the conductance retention is  $15.9\%$  and  $80.6\%$  for pure  $\text{ZnSO}_4$  electrolyte and  $\text{ZnSO}_4$  electrolyte with  $\text{MnSO}_4$  additive, respectively. Exhilaratingly, the conductance can be restored to initial level in  $\text{ZnSO}_4$  electrolyte with  $\text{MnSO}_4$  additive after the first galvanostatic charging process at  $1 \mu\text{A cm}^{-2}$ , indicating reversible structure evolution (Figure 3b). Nevertheless, the conductance recession was not completely reversible and could not be restored to the initial state even after deep galvanostatic charging in pure  $\text{ZnSO}_4$  electrolyte (Figure 3d). The long-term cycling performances of the ZIBs based on  $\text{MnO}_2$  LBNWs were also investigated in the above different electrolytes (Figure S6, Supporting Information). In detail,  $77.8\%$  and  $95.7\%$  of the initial capacity are retained at  $1 \mu\text{A cm}^{-2}$  over 375 charge/discharge cycles in pure  $\text{ZnSO}_4$  electrolyte and  $\text{ZnSO}_4$  electrolyte with  $\text{MnSO}_4$  additive, respectively. Corresponding to this result, the  $\text{MnO}_2$  LBNWs exhibit higher conductance retention in the preadded  $\text{Mn}^{2+}$  electrolyte compared with  $\text{ZnSO}_4$  electrolyte (Figure 3c,f). Notably, the conductance of the  $\text{MnO}_2$  LBNWs monotonically decrease along with the charge/discharge cycles rather than reversible transition in the above two electrolytes, which indicate the structure of the material has undergone permanent changes after long-term cycling. In situ Raman test gives further proof, which will be discussed later.

With the purpose of getting detailed information, a series of characterizations were carried out before/after electrochemical cycling (Figure 4). Transmission electron microscopy (TEM) presents a smooth shape of the  $\text{MnO}_2$  at the initial state (Figure 4a). After 375 charge/discharge cycles at  $1 \mu\text{A cm}^{-2}$  in preadded  $\text{Mn}^{2+}$  electrolyte, a rough layer with the thickness of  $5$ – $10 \text{ nm}$  appears at the surface of  $\text{MnO}_2$  LBNWs (Figure 4d). While the surface of partial  $\text{MnO}_2$  LBNWs become broken in pure  $\text{ZnSO}_4$  electrolyte (Figure 4b), which is consistent with a slippery slope in conductance of the electrode material (Figure 3e). The high-resolution transmission electron microscopy (HRTEM) images display a clear lattice fringes of  $\text{MnO}_2$  LBNWs after long cycling with spacing of about  $0.260$  and  $0.249 \text{ nm}$ , corresponding to the (210) plane of  $\text{MnOOH}$  (JCPDS No. 00-074-1049) and the (211) plane of  $\text{Mn}_2\text{O}_4$  (JCPDS No. 00-016-0154), respectively. The outer coating layer presents an amorphous shape. The selected area electron diffraction (SAED) pattern (Figure 4e) reveals the single-crystalline nature of the interior nanowire. As shown in energy-dispersive spectroscopy (EDS) (Figure 4c,f), the results clearly indicate that Zn element is distributed homogeneously in  $\text{MnO}_2$  nanowires after long-term cycling. Furthermore, X-ray photoelectron spectroscopy (XPS) analyses also confirm that Zn element is distributed in  $\text{MnO}_2$  nanowires (Figure S8, Supporting Information). For circulating electrode material, the Zn 2p XPS spectroscopy (Figure S8a, Supporting Information) shows that the peaks at  $1022.87$  and  $1045.97 \text{ eV}$  correspond to Zn  $2p_{1/2}$  and Zn  $2p_{3/2}$ , respectively.

To further reveal the energy storage behavior during charge/discharge processes, confocal in situ Raman spectroscopy

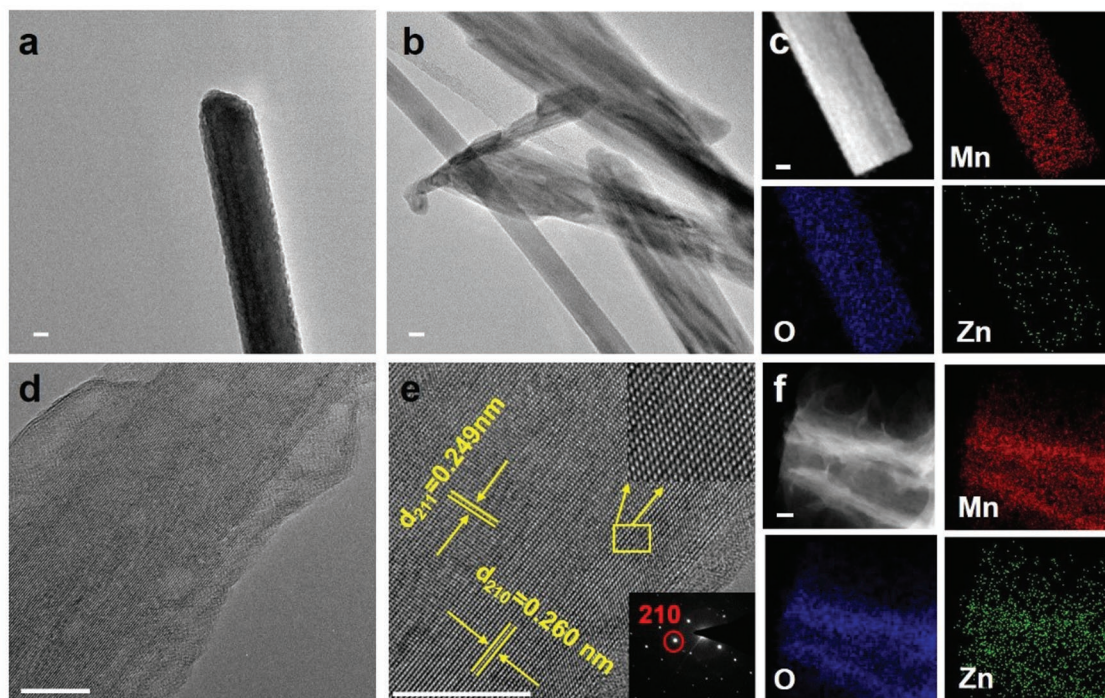


**Figure 4.** TEM characterization of MnO<sub>2</sub> LBNWs before and after electrochemical long-term cycling in different electrolytes. a) TEM image of MnO<sub>2</sub> LBNWs at initial state. b,c) TEM image and EDS mapping images of MnO<sub>2</sub> LBNWs after 375 charge/discharge cycles at 1 μA cm<sup>-2</sup> in pure ZnSO<sub>4</sub> electrolyte. d–f) TEM image and EDS mapping images of MnO<sub>2</sub> LBNWs after 375 charge/discharge cycles at 1 μA cm<sup>-2</sup> in ZnSO<sub>4</sub> electrolyte with MnSO<sub>4</sub> additive. All the scale bars are 10 nm.

was conducted (Figure 5). For the in situ Raman measurements, MnO<sub>2</sub> LBNWs attached to pyrolytic carbon as cathode, 2 M ZnSO<sub>4</sub> electrolyte with 0.1 M MnSO<sub>4</sub> additive as electrolyte, and ultrafine zinc rod as anode were assembled. Initially, all apparent Raman bands are consistent well with MnO<sub>2</sub>. Among them, the Raman band at 632 cm<sup>-1</sup> is assigned to symmetric Mn–O vibration in the MnO<sub>6</sub> octahedral and the Raman band at 580 cm<sup>-1</sup> is assigned to Mn–O vibration which reveal a well-developed tetragonal structure composed of interstitial space of (2 × 2) tunnel. The low-frequency Raman band at 176 cm<sup>-1</sup> is related to external vibration of the MnO<sub>6</sub> octahedra.<sup>[30,31]</sup> When the MnO<sub>2</sub> LBNW devices were discharged to 1.4 V (State I to state III in Figure 5), there was no obvious change of the typical peaks. Notably, Raman bands at 552, and 148 cm<sup>-1</sup> aroused from State IV to VI, result from the formation of MnOOH, which is caused by the insertion of proton during the discharge processes. The oxidation state of the Mn element was progressively lowered, resulting in a smaller ionic radius and short length of Mn–O band, thus inducing the blue shift of the band at 583 cm<sup>-1</sup>. In addition, we observed a strong band at 655 cm<sup>-1</sup>, which is the characteristic band of Mn<sub>3</sub>O<sub>4</sub> spinel structure. The peak is attributed to the A<sub>1g</sub> mode, which corresponds to the Mn–O respiratory vibration of the tetrahedral coordination, indicating the presence of Mn<sub>3</sub>O<sub>4</sub> phase.<sup>[25]</sup> On the contrary, the Raman bands at 552, 148, and 655 cm<sup>-1</sup> gradually decreased from State VI to State IX, resulting in the reversible transformation from MnOOH and Mn<sub>3</sub>O<sub>4</sub> to α-MnO<sub>2</sub> during the charge processes. When charged to 1.6 V, the Raman spectroscopy indicates a completely reversible structure

evolution. Interestingly, instead of reversible change, the Raman spectroscopy after long-term cycling shows severe irreversibility (Figure S9, Supporting Information). This observation of Raman spectroscopy agrees with the conductance variation in Figure 3.

We revealed the phase transition mechanism of Zn–MnO<sub>2</sub> by combining electrochemical and physical techniques, including TEM, XPS, in situ Raman, and *I–V* analysis. After shallow discharging process, spectroscopy characterization results show that α-MnO<sub>2</sub> is converted to MnOOH and Mn<sub>3</sub>O<sub>4</sub>, which is accompanied with the conductance decrease of MnO<sub>2</sub> LBNWs. Exhilaratingly, MnOOH and Mn<sub>3</sub>O<sub>4</sub> reversibly converting to α-MnO<sub>2</sub> completely is observed along with the increase of the conductance. The conductance of the material plays a vital role in battery performance. It can thus be concluded that the phase transition is mainly responsible for the capacity degradation of Zn–MnO<sub>2</sub>. In addition, we observed that permanent phase transition of α-MnO<sub>2</sub> occurs after deeply discharging process, in correspondence with severe deterioration of conductance and capacity. More importantly, preadded Mn<sup>2+</sup> can effectively maintain the high conductance and capacity of MnO<sub>2</sub> LBNWs by inhibiting the dissolution of manganese ions.

### 3. Conclusion

In summary, we reported an on-chip LBS approach for directly probing the conductance change and structural evolution of electrode materials in battery cycling process. First, a facile

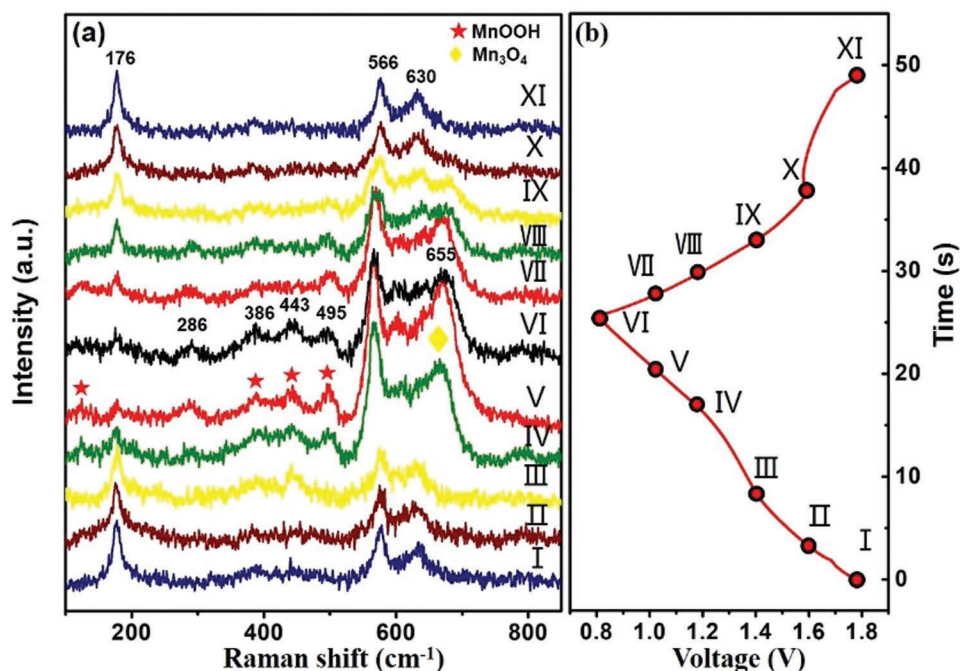


**Figure 5.** In situ Raman characterization of LBNW devices. a) Raman spectroscopy evolution of  $\text{MnO}_2$  LNNWs at different charge/discharge states. b) Corresponding galvanostatic charge and discharge curves at  $1 \mu\text{A cm}^{-2}$ .

Langmuir–Blodgett process was studied which can effectively avoid introducing binders and conductive carbon additives. Second, pyrolytic carbon was selected as current collector which can simulate the real environment of battery operation due to small interface impedance. Electrical transport studies and in situ  $I$ – $V$  test offer complementary information compared with conventional characterization techniques for in-depth understanding of reaction. Our study thus offers an effective approach to determine suitable current collectors possessing optimum electrical contact and defining a specialized electrode material platform for both basic electrical and electrochemical studies. Application to a study of electrochemical reactions based on  $\text{MnO}_2$  electrode has been confirmed that a reversible phase transition from  $\text{MnO}_2$  to  $\text{MnOOH}$ ,  $\text{Mn}_3\text{O}_4$  occurs during charge/discharge processes. LBNW energy device provides a great micro/nano-scale battery diagnostic platform to stimulate the further development of nanowire electrode materials and has the potential to build self-powered integrated nanochips.

#### 4. Experimental Section

**Synthesis of  $\text{MnO}_2$  Nanowires:** The single crystalline  $\text{MnO}_2$  nanowires were synthesized by a hydrothermal method according to the previous work.<sup>[9]</sup> 2 mmol  $\text{KMnO}_4$  (Sigma Aldrich) and 2 mmol  $\text{NH}_4\text{F}$  (Sigma Aldrich) were added into the distilled (DI) water to reach the total volume of 80 mL. The precursor was stirred for 20 min, then transferred to a 100 mL Teflon lined autoclave, and kept in an oven at  $180^\circ\text{C}$  for 24 h. The product was washed and dried to get  $\text{MnO}_2$  nanowires.

**Preparation of Freestanding LBNW Film:** A freestanding Langmuir–Blodgett nanowire (LBNW) film was assembled by LBS. Typically,  $\text{MnO}_2$  nanowires suspension in ethanol (500 mL,  $0.4 \text{ mg mL}^{-1}$ ) was mixed with DI water (500 mL) and *n*-butanol (Sigma Aldrich) (300 mL). The obtained  $\text{MnO}_2$  nanowires suspension was added drop by drop into

a flask (about 5 cm in diameter) filled with DI water. A film of  $\text{MnO}_2$  nanowires was then formed on the surface and was later transferred onto the silicon wafer.

**Device Fabrication:** For the fabrication of microelectrodes, SU-8 2000.5 photoresists were first coated on silicon wafers (with a 300 nm  $\text{SiO}_2$  layer) by spin coating. The silicon wafers were then exposed to ultraviolet light for 45 s, and the patterned silicon wafers were obtained after developing and rinsing. The assembling methods of different current collectors were as follows: i) obtaining the patterned electrodes by removing excess photoresist by SU-8 developer. During the carbonization process, the temperature of tube furnace increased to  $400^\circ\text{C}$  at a rate of  $1^\circ\text{C min}^{-1}$ , and kept at this temperature for 30 min, then increased to  $900^\circ\text{C}$  at a rate of  $2^\circ\text{C min}^{-1}$ , and kept at  $900^\circ\text{C}$  for 1 h in  $\text{N}_2$  air, and finally tube furnace cooled to room temperature naturally. ii) 5 nm Cr and 50 nm Au were deposited on the silicon wafers by physical vapor deposition. The silicon wafers patterned with the 5 nm Cr and 50 nm electrodes were then obtained after removing the photoresists with SU 8 developer. iii) 50 nm Ti were deposited on the silicon wafers by physical vapor deposition. The silicon wafers patterned with the 50 nm Ti electrodes were then obtained after removing the photoresists with SU 8 developer. The prepared (by Langmuir–Blodgett scooping) freestanding film of  $\text{MnO}_2$  nanowires was then deposited onto the substrate surface.

**In situ Device Characterization:** In the in situ  $I$ – $V$  test, the probe station was used. The first set of probes was used to collecting the conductance of the nanowires at different charge/discharge states. The second set of probes was used to supply a small potential (100 mV) between source and drain electrodes. For the in situ Raman measurements,  $\text{MnO}_2$  LBNWs attached to pyrolytic carbon as cathode,  $\text{ZnSO}_4$  electrolyte with  $\text{MnSO}_4$  additive as electrolyte, and ultrafine zinc rod as anode were assembled. Raman spectroscopy was recorded using a Renishaw RM-633 laser. Meanwhile, the CV measurement was carried out in the scan rate of  $0.2 \text{ mV s}^{-1}$ . The SEM images of the samples were observed by a JEOL JSM-7100F scanning electron microscope. EDS were collected by an Oxford IE250 system. Transmission electron microscope (TEM) images were collected using Titan G2 60-300 Probe Cs Corrector HRSTEM. X-ray diffractometer characterizations were collected using a

D8 Discover X-ray diffractometer with Cu K $\alpha$  radiation ( $\lambda = 1.054056 \text{ \AA}$ ). XPS measurements were performed with a VG MultiLab 2000 instrument. The thicknesses of microelectrodes were measured by stylus surface profiler (Bruker Dektaker TX).

## Supporting Information

Supporting Information is available from the Wiley Online Library or from the author.

## Acknowledgements

This work was supported by the National Natural Science Foundation of China (51802239, 51832004), the National Key R&D Program of China (2016YFA0202603), the National Natural Science Fund for Distinguished Young Scholars (51425204), the National Basic Research Program of China (2013CB934103), and the Fundamental Research Funds for the Central Universities (2019IVB054, 2019III062) [L].

## Conflict of Interest

The authors declare no conflict of interest.

## Keywords

electrical transport, manganese dioxide, nanowire assembly, Zn-ion batteries

Received: April 29, 2019

Revised: May 17, 2019

Published online:

- [1] J. M. Tarascon, M. Armand, *Nature* **2001**, 414, 359.  
 [2] M. Armand, J. M. Tarascon, *Nature* **2008**, 451, 652.  
 [3] J. W. Choi, D. Aurbach, *Nat. Rev. Mater.* **2016**, 1, 16013.  
 [4] H. Pan, Y. Shao, P. Yan, Y. Cheng, K. S. Han, Z. Nie, C. Wang, J. Yang, X. Li, P. Bhattacharya, K. T. Mueller, J. Liu, *Nat. Energy* **2016**, 1, 16039.  
 [5] K. Haegyeom, H. Jihyun, P. Kyu-Young, K. Hyungsub, K. Sung-Wook, K. Kisuk, *Chem. Rev.* **2014**, 114, 11788.  
 [6] K. Karki, E. Epstein, J. H. Cho, Z. Jia, T. Li, S. T. Picraux, C. Wang, J. Cumings, *Nano Lett.* **2012**, 12, 1392.  
 [7] H. Chang, H. Wu, *Energy Environ. Sci.* **2013**, 6, 3483.  
 [8] M. Shao, Q. Chang, J. P. Dodelet, R. J. C. R. Chenitz, *Chem. Rev.* **2016**, 116, 3594.  
 [9] P. Hu, M. Yan, X. Wang, C. Han, L. He, X. Wei, C. Niu, K. Zhao, X. Tian, Q. Wei, Z. Li, L. Mai, *Nano Lett.* **2016**, 16, 1523.  
 [10] N. Zhang, F. Cheng, J. Liu, L. Wang, X. Long, X. Liu, F. Li, J. Chen, *Nat. Commun.* **2017**, 8, 405.  
 [11] V. Soundharajan, B. Sambandam, S. Kim, M. H. Alfaruqi, D. Y. Putro, J. Jo, S. Kim, V. Mathew, Y. K. Sun, J. Kim, *Nano Lett.* **2018**, 18, 2402.  
 [12] C. Xu, B. Li, H. Du, F. Kang, *Angew. Chem., Int. Ed.* **2012**, 51, 933.  
 [13] D. Xu, B. Li, C. Wei, Y. B. He, H. Du, X. Chu, X. Qin, Q. H. Yang, F. Kang, *Electrochim. Acta* **2014**, 133, 254.  
 [14] R. Trócoli, M. F. La, *ChemSusChem* **2015**, 8, 481.  
 [15] M. A. González, R. Trócoli, I. Pavlovic, C. Barriga, F. L. Mantia, *Electrochem. Commun.* **2016**, 68, 1.  
 [16] B. Häupler, C. Rössel, A. M. Schwenke, J. Winsberg, D. Schmidt, A. Wild, U. S. Schubert, *NPG Asia Mater.* **2016**, 8, e283.  
 [17] D. Kundu, B. D. Adams, V. Duffort, S. H. Vajargah, L. F. Nazar, *Nat. Energy* **2016**, 1, 16119.  
 [18] H. Liu, Y. Zou, L. Tao, Z. Ma, D. Liu, P. Zhou, H. Liu, S. Wang, *Small* **2017**, 13, 29.  
 [19] D. Wang, H. Li, Z. Liu, Z. Tang, G. Liang, F. Mo, Q. Yang, L. Ma, C. Zhi, *Small* **2018**, 14, 24.  
 [20] L. Mai, Y. Dong, L. Xu, C. Han, *Nano Lett.* **2010**, 10, 4273.  
 [21] Y. Lu, Y. Yang, A. Sellinger, M. Lu, J. Huang, H. Fan, R. Haddad, G. Lopez, A. R. Burns, D. Y. Sasaki, *Nature* **2001**, 410, 913.  
 [22] X. Li, G. Zhang, X. Bai, X. Sun, X. Wang, E. Wang, H. Dai, *Nat. Nanotechnol.* **2008**, 3, 538.  
 [23] X. Chen, S. Lenhart, M. Hirtz, N. Lu, H. Fuchs, L. Chi, *Acc. Chem. Res.* **2010**, 38, 393.  
 [24] M. S. Kim, J. H. Ryu, Y. R. Lim, I. W. Nah, K. R. Lee, L. A. Archer, W. I. Cho, *Nat. Energy* **2018**, 3, 889.  
 [25] H. L. Nie, X. Dou, Z. Tang, H. D. Jang, J. Huang, *J. Am. Chem. Soc.* **2015**, 137, 10683.  
 [26] X. Fanton, A. M. Cazabat, *Langmuir* **1998**, 14, 2554.  
 [27] C. V. Sternling, L. E. Scriven, *AIChE J.* **1959**, 5, 514.  
 [28] X. Xia, H. Li, Z. H. Chen, *J. Electrochem. Soc.* **1989**, 136, 266.  
 [29] M. S. M. Ata, *Carbon* **2001**, 39, 1913.  
 [30] S. Cheng, L. Yang, D. Chen, X. Ji, Z. j. Jiang, D. Ding, M. Liu, *Nano Energy* **2014**, 9, 161.  
 [31] D. Chen, D. Ding, X. Li, G. H. Waller, X. Xiong, M. A. El-Sayed, M. Liu, *Chem. Mater.* **2015**, 27, 6608.